Deep Clustering in Radar Subglacial Reflector Reveals New Subglacial Lakes

Sheng Dong[1,2], Lei Fu[3,*], Xueyuan Tang[2,4,*], Zefeng Li[1], and Xiaofei Chen[5]

[1]School of Earth and Space Sciences, University of Science and Technology of China, Hefei, China
[2]Key Laboratory of Polar Science, MNR, Polar Research Institute of China, Shanghai, China
[3]School of Geophysics and Geomatics, China University of Geosciences, Wuhan, China
[4]School of Oceanography, Shanghai Jiao Tong University, Shanghai, China
[5]Department of Earth and Space Sciences, Southern University of Science and Technology, Shenzhen, China

Correspondence: Lei Fu (fulei@cug.edu.cn) and Xueyuan Tang (tangxueyuan@pric.org.cn)

Abstract. Ice-penetrating radar (IPR) imaging is a valuable tool for observing the internal structure and bottom of ice sheets. Subglacial water bodies, also known as subglacial lakes, generally appear as distinct, bright, flat, and continuous reflections in IPR images. In this study, we collect and generate a dataset of one-dimensional reflector waveform features from IPR images of the Gamburtsev Subglacial Mountains region in the CReSIS database, to investigate these features. We apply a deep

5   learning method to reconstruct the reflector features, and subsequently downsample the features to a low-dimensional vector representation. An unsupervised clustering method is then used to separate different types of reflector features, including a reflector type corresponding to subglacial water bodies. The derived clustering labels are used to detect features of subglacial water bodies in IPR images. Using this method, we compare the new detections with the known lakes inventory. The results indicate that this new method identified additional subglacial lakes that were not previously detected, and some previously

10 known lakes are found to correspond to other reflector clusters. This method can offer automatic detections of subglacial lakes and provide new insight for subglacial studies.

1 Introduction

Subglacial water exists between bedrock and glacier or ice sheet is formed through a complex interplay of factors such as subglacial pressure, friction heat, geothermal flux, and surface water injection (Robin et al., 1970; Siegert, 2000; Pattyn, 2010).

15 Subglacial lakes play an important role in subglacial water networks, which can also impact ice flow and dynamics (Kamb, 1987; Stearns et al., 2008; Siegfried et al., 2016). Investigation of water storage in subglacial lakes can provide insights into the history of former climate change and ice sheet evolution (Dowdeswell and Siegert, 1999) and estimate the contribution of ice sheet meltwater to sea level rise (King et al., 2020; Fettweis et al., 2013). In addition, the extreme conditions of low temperature and absent sunlight create unique subglacial lacustrine ecosystems (Christner et al., 2014; Mikucki et al., 2016).

20 Subglacial lake sediments may also contain information that records the historical evolution of ice sheets (Smith et al., 2018).

Ice-penetrating radar technology has in recent years allowed the detection of the subsurface feature of ice sheets (Carter et al., 2007; Paden et al., 2010; Arnold et al., 2020). Subglacial water bodies can be identified in radar images due to their

distinct, bright, flat, and specular reflection characteristics (Oswald and Robin, 1973). Active seismic surveys are also utilized to investigate the thickness of the subglacial water layer and sediment characteristics at the bottom of lakes (Paden et al., 2010;
25 Arnold et al., 2020). Gravimetry and electromagnetic methods have also been employed to study subglacial lakes (Studinger et al., 2004; Key and Siegfried, 2017).These observations have been used to construct the first Global Subglacial Lake Inventory (Livingstone et al., 2022).

Because of the specific reflection characteristics of subglacial water bodies in IPR images (Schroeder et al., 2013), the manual extraction of the visual features was initially applied (Siegert and Ridley, 1998; Gades et al., 2000; Dowdeswell and
30 Evans, 2004). With the increase in IPR data, semi-automatic methods based on ice-bottom roughness features and reflected signal power have been developed to search for lake candidates (Carter et al., 2007; Bowling et al., 2019). Automatic methods based on experts' experience and physical modeling (Lang et al., 2022; Hao et al., 2023), as well as machine learning methods (Gifford and Agah, 2012; Ilisei et al., 2018) have also been proposed in subglacial water body detection. These methods have shown that improved selection rules and thresholds can enhance detection accuracy and efficiency. However, the new
35 rules based on experience or physical model assumptions depend on subjective factors and may lead to potential inaccurate detections in the absence of a complete interpretation of basal radar reflectance features.

In recent years, Deep learning (DL) has been applied as a powerful tool for automated layer features extraction in radar images, including bedrock interfaces (Xu et al., 2017; Rahnemoonfar et al., 2017; Dong et al., 2021; Liu-Schiaffini et al., 2022), internal ice layers (Yari et al., 2020; Varshney et al., 2020; Dong et al., 2021), snow accumulation layers (Varshney
40 et al., 2021), and radar semantic segmentation (García et al., 2021; Ghosh and Bovolo, 2022). Additionally, DL-based methods are also developed for subglacial feature identification (Gifford and Agah, 2012; Ilisei and Bruzzone, 2015; Ilisei et al., 2018), which have improved the efficiency of IPR image interpretation (Wang et al., 2023). These DL-based automated approaches have effectively expanded the ice thickness catalog and enabled further data applications in ice sheet studies (e.g., Tang et al., 2022; Wang et al., 2023).

45 The Center for Remote Sensing and Integrated Systems (CReSIS) released an extensive collection of historical radar images recorded in the Antarctic and Greenland ice sheet (Arnold et al., 2020). These datasets have driven various investigation of recent subglacial studies (e.g., Varshney et al., 2021; Zeising et al., 2022). By utilizing the precise label in the CReSIS dataset for reflectors from ice bottom, it is now feasible to construct a comprehensive catalog of basal reflector characteristics, facilitating further analysis of reflector features.

50 In this study, we use IPR images from the CReSIS captured near the Gamburtsev Subglacial Mountains to construct a waveform dataset of 1-D ice bottom reflector characteristics. Using this dataset, we train a Variational Auto-Encoder (VAE, Kingma and Welling, 2013) to reconstruct the time-domain waveform features of basal reflectors. We then apply K-means clustering method (MacQueen, 1967) in the VAE's latent space to analyze similar reflection features and separate them into different clusters. We notice a cluster of reconstructed reflectors with sharp, steep, and symmetric waveform characteristics
55 corresponding to the features observed in field radar images. Furthermore, we apply a conventional method based on the linear relationship between depth and peak reflected power to filter the candidate subglacial water bodies from latent space clustering. By using this workflow, we can obtain an automatic approach in subglacial water bodies detection. To validate the

results, we compare the distributions of subglacial water bodies by this method with the existing inventories. This new method can improve the efficiency and accuracy of the detection of subglacial water bodies and also provides a potential application to extract reflectors with similar waveform characteristics as water bodies. Additionally, this approach can be extended to detect and label the other clusters of subglacial features, providing valuable reference data for further studies of subglacial environments.

2   Data and Methods

In this section, we will introduce the workflow of the ice bottom reflection feature clustering method, as shown in Figure 1, which includes the extraction and sampling of ice bottom reflector features (Figure 1a), the feature reconstruction and latent vector encoding reduction by variational auto-encoder (Figure 1b), the unsupervised clustering of ice bottom reflector features (Figure 1c), and the implementation of labeling for subglacial water bodies (Figure 1d).
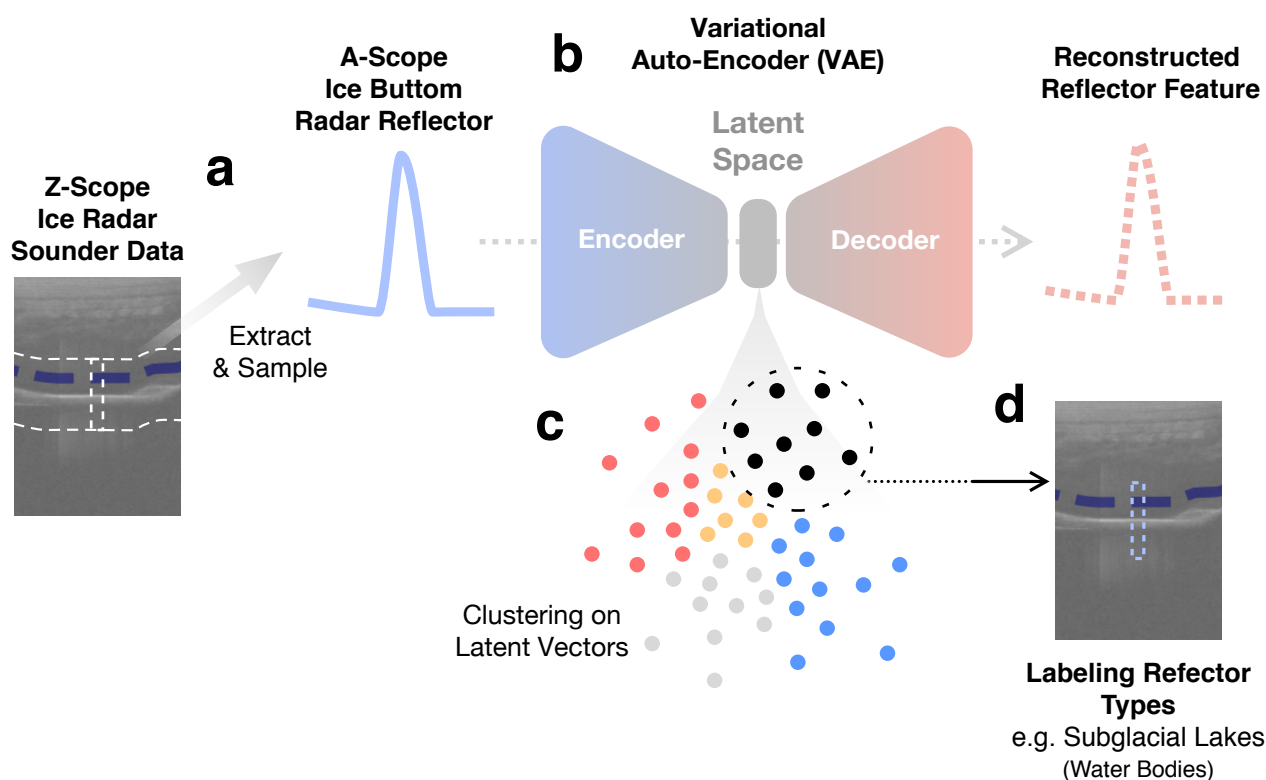
Figure 1. Workflow for subglacial water bodies detection: (a) Extract and sample the ice bottom reflector trace by trace in IPR images. (b) VAE reconstructs and encoding of the sampled ice bottom reflector features. (c) Supervised clustering on the encoded latent vectors. (d) Trace the ice bottom reflector corresponding to the subglacial water bodies cluster.

2.1 Ice bottom reflectors

We follow the known lakes inventories (Wolovick et al., 2013; Livingstone et al., 2022) to investigate subglacial water bodies
70 in the Gamburtsev Subglacial Mountains region. The utilized airborne radar images were collected during the December 2008-
January 2009 Antarctic's Gamburtsev Province Project (AGAP) from the CReSIS database. According to the lakes inventory,
multiple known subglacial lakes are located in this study area. We focus on the dataset from the southern camp of Dome A
(AGAP-S), which comprises 2,715 IPR images with a central frequency of 150 Hz, a bandwidth of 10 MHz, and a transmitting
power of 800 W (Wolovick et al., 2013). The radar data were acquired from L1B data product (CSAPR_standard), which
75 employs focused synthetic aperture radar processing on each channel and motion compensation during data pre-processing
(Arnold et al., 2020). The radar images have an average spatial along-track trace spacing of 1.3 m and a time sample step of
10^{-7} s, equivalent to a sample range of 8.4 m in ice. The radar images also contain the positions of ice bottom reflectors, which
were extracted by hybrid manual-automatic method(Wolovick et al., 2013).

In this study, we perform a series of data processing steps to extract the ice bottom reflector signals from the radar images.
80 First, we transfer the echo power to decibel scale for each radar image by $[X]_{db} = 10 * \log_{10}(X)$, where X is the pixel value
from the images. Second, we apply the reflector position markers in the dataset to truncate the 1-D data within the ± 200
sampling points near the reflector position for every single trace along Z-axis. Third, we align the 1-D trace data by centering
the traces according to their maximum value (peak echo) to correct minor position misfits of semi-automatic reflector picking.
This step ensures that the maximum value of bottom reflector signal features always resided at the center of the 1-D trace data.
85 Finally, we truncate ± 64 data sampling points around the peak signal centers, which maintain a fixed length of 128 for each
ice-bottom reflection signal. As the sampling rates of the radar images in this region are identical, the sample ranges of the ice
bottom reflector features are also consistent.

To enhance the reflector features and minimize the impact of sampling noise in radar images, a constant Gaussian filter is
applied to all the extracted trace reflector data. Last, all reflector features from different radar images are normalized to reduce
90 the influence of background echo power in the radar image and accentuate the reflector features. By following the steps above,
we collect and generated an ice bottom reflector waveform feature dataset with 1488600 1-D Z-axis (A-Scope) radar echo
traces.

2.2 Variational Auto-Encoder

Variational Auto-Encoder (VAE) was first proposed by Kingma and Welling (2013) and designed for image and signal process-
95 ing. As an auto-encoder, VAE consists of an encoder and a decoder: the encoder reduces the data sizes and downsamples the
input data to vectors in latent space; the following decoder reconstructs the latent vectors to approach and match the raw input
data. After training, the encoded latent vectors can be considered dimension-reduced representations of the input data. And the
reconstructed data from the decoder can trace and reveal the correlation between the sampled vectors in the continuous latent
space. VAE now has various applications in Earth science studies, such as geophysical inversion (Cheng and Jiang, 2020; Liu

100 et al., 2022; Lopez-Alvis et al., 2021), shale petroleum prediction (Li and Misra, 2017), engineering seismic analysis(Esfahani
et al., 2021) and seismic mechanism analysis (Li, 2022; Ma et al., 2022).

In this study, we employ VAE to reconstruct the reflector waveform features from the ice bottom. The VAE architecture
is shown in Figure 2a, which consists of fully connected layers, including an input layer of 128 neurons, an encoder and a
decoder consisting of two hidden layers with 128 neurons, and an output layer with 128 neurons. To visually present spatial

105 distributions of the latent vectors, we design the bottleneck (latent space) between the encoder and decoder to a small size of 2
* 1. The loss function used in VAE training follows Kingma and Welling (2013) and Li (2022):

$$\text{Loss} = \text{MSE} + \text{KL} \tag{1}$$

where the MSE measures the average difference between the predicted and actual values, while the KL represents Kull-
back–Leibler divergence, which measures the dissimilarity between the probability distribution of the Latent Space and a

110 Gaussian distribution:

$$\text{MSE} = ||X' - X|| \tag{2}$$

$$\text{KL} = -0.5 \cdot \sum_{i=1}^{n} (1 + \log(\sigma_i^2) - \mu_i^2 - \sigma_i^2) \tag{3}$$

where X and X' are raw input reflectors and VAE reconstructed reflectors respectively. The MSE in loss function is applied to

115 calculate reconstruction misfit and KL divergence for estimating and reducing the difference between the distribution and the
normal distribution in latent space. N represents the dimension of the latent space Z, which was preset to 2 in this study, and
σ and μ are the variance and mean of the latent space respectively. The Adam Optimizer (Kingma and Ba, 2014) is employed
to accelerate the training process.

We use the randomly shuffled reflector datasets to train and validate VAE. 90% of the data are used for training VAE, while

120 the remaining 10% served as a validation set. The VAE is updated by a full training dataset during different epochs in training.
Due to the similar reflector features and large data amount applied in training, the training loss rapidly descends and no longer
changes after epoch 4, therefore we stop training at epoch 10.

To evaluate the VAE's reconstruction performance, we randomly select different reflectors from the validation set to demon-
strate the reconstruction of ice bottom reflector features (Figure 2b, c). Subfigures in figure 2b show a group of symmetrical

125 reflectors and their corresponding reconstruction. The reconstructed reflector features (orange waveforms) remain the width
and trend of raw input reflector features (blue waveforms). Due to the low-dimension bottleneck with 2*1 size applied in the
latent space, the high-frequency detailed features in reflectors feature are unattainable and thus discarded by VAE. Figure 2c
demonstrated a group of asymmetric reflector features and the corresponding VAE reconstruction. The comparison between
inputs and reconstructions suggests that the asymmetric trends of the reflector feature are also successfully reconstructed, as

130 well as the width waveform feature. In general, VAE can reconstruct the features of both symmetric and asymmetric ice bottom
reflectors. Furthermore, we select typical reflectors with large reconstruction errors to demonstrate the large misfit conditions
(Figure 2d). Notably, reflectors contained with high-frequency signals, multiple peaks, and severe oscillations are challenging
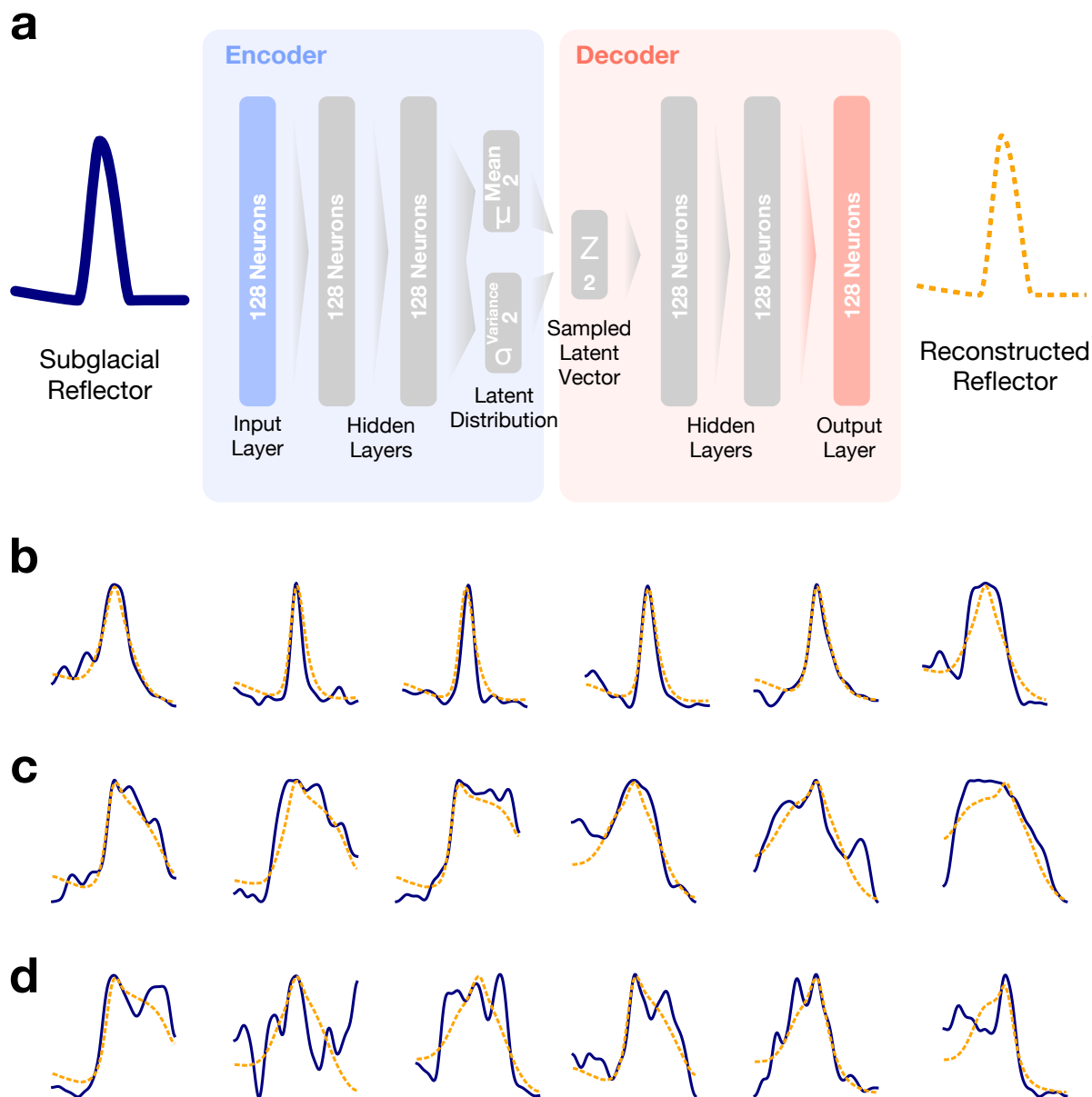
Figure 2. Variational Auto-Encoder (VAE) and demonstrations of ice bottom reflector reconstruction. (a) VAE architecture, with both encoder and decoder consisting of two fully connected layers with 128 neurons, and bottleneck 1×2 latent space. (b-d) Demonstrations of data reconstruction using VAE: input raw reflectors (blue waveforms) and VAE reconstructed reflectors (orange waveforms). (b) Symmetrical reflector features. (c) Asymmetrical reflector features. (d) complex reflector features, which result in higher reconstruction errors by VAE.

to be reconstructed, thus resulting in higher errors. These peculiar signal features deviate significantly from the majority of reflector features in the training set, rendering the features difficult to encode and decode through latent vectors. The recon-

135   structions of multiple peak features are usually simplified to broader reflection shapes, whose trends are approximate to the smooth shape and average of the input features.

As shown in Figure 2a, the original 128-length reflector waveform features are transformed into a 2-length latent vector between the encoder and decoder of the VAE. The features of ice bottom reflectors are derived by the encoder part of the VAE to latent vectors consisting of two dimensionless scalars, Z_1 and Z_2, which can be regarded as vectors containing the original

140   signal features. Therefore, the distance between vectors in the latent space can be considered as an indicator of statistical feature similarity.

2.3   Clustering Analysis in Latent Space

After VAE training, we randomly select a subset with 2000 reflector samples from the intact dataset to validate the encoder. Because the selection is uniformly random, the reflector samples are from different radar images captured in different regions,

145   and thus the samples reveal different ice bottom conditions. The reflector samples are first encoded by VAE's encoder to 2-D vectors in latent space. Figure 3a shows the vector distributions of the samples in the latent space, in which each scattered point corresponds to an encoded reflector sample. Due to the application of KL divergence in VAE's loss function, the vector distribution of these samples in the latent space composed of Z_1 and Z_2 is approximate to a 2-D Gaussian distribution. According to the character of VAE Kingma and Welling (2013), the distance between encoded vectors in the latent space is equivalent to the

150   difference between the input reflector samples. Thus, analyzing the latent spatial relationships of the vectors in the latent space enables us to explore potential relationships between the corresponding reflector features. By applying a clustering method in the sample-encoded vectors in latent space, we can furthermore separate different types with similar ice bottom reflector features.

To improve the clustering efficiency, it is advisable to reduce the amount of data used. However, in order to ensure the accu-

155   racy of clustering, the selected samples should have sufficient data density and match the same distribution as the experimental data. As illustrated in Figure 3a, using latent vectors from a randomly selected set of 2000 reflectors is sufficient for clustering. Therefore, we apply these samples for the next clustering analysis. We employ the K-means clustering algorithm (MacQueen, 1967), which based on the Euclidean distance estimation of the differences between data samples, as well as the characteristics in VAE's latent space. Initially, K clustering centers are randomly assigned in 2-D space. The distance of each sample vector to

160   the cluster center is computed, and the sample is assigned to the nearest cluster with the smallest distance. Then, all the cluster centers are updated to the spatial center of all the samples belonging to the corresponding cluster. This assign-update process is repeated until the cluster center becomes constant or the clustering result remains unchanged.

The number of clusters (K) is a preset parameter in the K-means algorithm, which must balance the tradeoff between implied feature classes and feature density in the data. On the one hand, K should be sufficiently large to distinguish between different

165   ice bottom conditions. On the other hand, K should not be so large as to create unnecessary subclasses. To obtain optimal clustering results, we applied the elbow method to determine the appropriate value of K (as shown in Figure S1). However, the
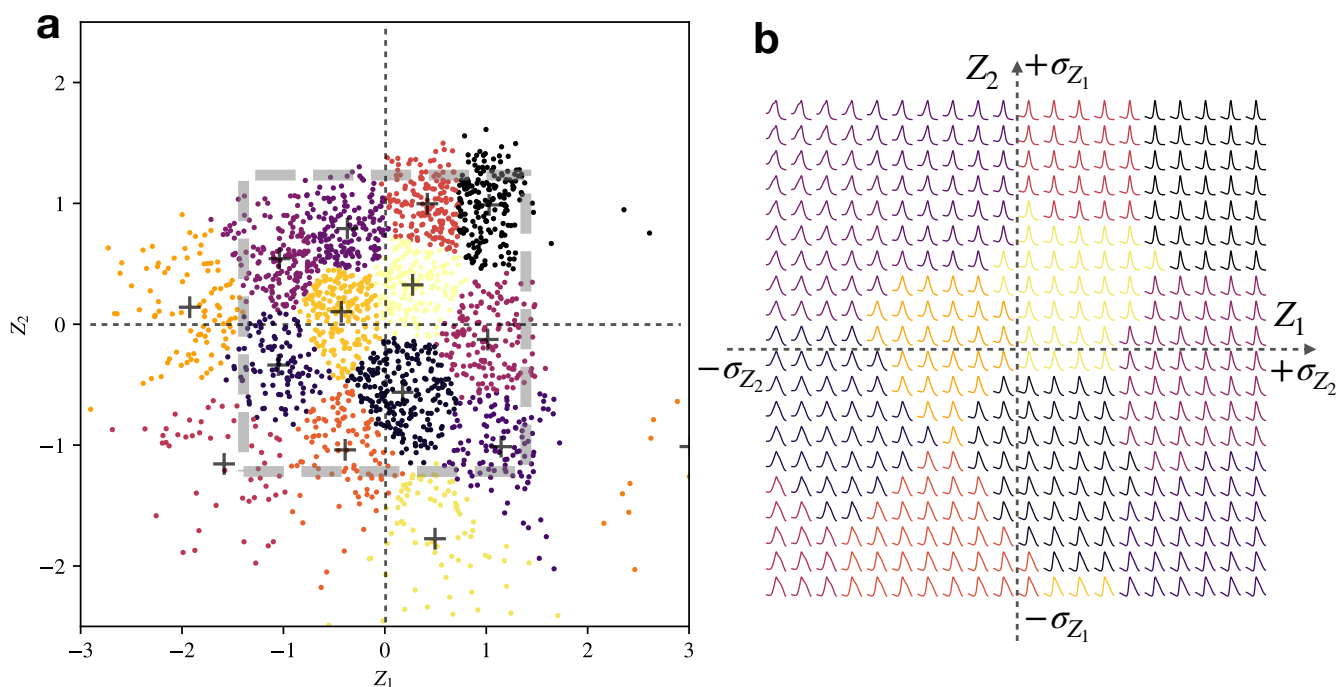
Figure 3. (a) Latent space distribution of 2000 randomly selected encoded reflector features, with each point representing an encoded reflector sample. The color of each point represents different clustering results (classes), and the black cross denotes the clustering center of each class. The gray dashed rectangle indicates the range of 2 standard deviations ($\pm\sigma_{Z_1}$ and $\pm\sigma_{Z_2}$) of the latent vectors. (b) Synthetic ice bottom reflectors reconstructed by virtual vectors, where the virtual vectors' range corresponds to the ranges of standard deviations (σ_{Z_1} and σ_{Z_2}). Different colors of the waveform correspond to different classes, with the candidate cluster corresponding to subglacial water bodies shown in black color near the upper right corner.

elbow curve does not show a clear cutoff point, possibly due to the distribution of vectors in the latent space (Figure 3a) not displaying a distinct trend of multiple classes. Therefore, we tested various alternative values of K, and ultimately selected $K = 15$. The clustering in latent vectors effectively separates the ice bottom reflector features corresponding to different conditions,
170 as demonstrated by the different colors of points in Figure 3a.

To visualize and investigate the latent spatial relationship between the ice bottom reflector features, we apply a set of virtual vectors by a grid with the same step length in the latent space. The synthetic ice bottom reflector feature of each vector can be obtained by inputting the vector into the decoder. The 2-D range of the virtual vector grid is assigned based on the standard deviation (σ) of Z_1 and Z_2, as shown in the gray dashed rectangle in Figure 3a. The grid is constructed by dividing Z_1 and
175 Z_2 into 20 intervals each, ranging from $-\sigma$ to $+\sigma$, with the same step size. By applying the 20×20 virtual grid to the VAE's decoder, we can obtain the generated synthetic ice bottom reflectors for each vector in the grid, as shown in Figure 3b.

The encoder-decoder trained on a large amount of data can obtain the performance in mapping latent vectors to the reflector features. Therefore, the ice bottom reflectors generated from virtual vectors also have similar features of symmetry, asymmetric tilt, and different widths as shown in Figure 2. Furthermore, the K-means clustering derived from the selected samples also

180 classifies the virtual latent vectors, and the classification results of different virtual reflectors are shown in different colors in Figure 3b. Within the same cluster in the latent space, the reflector features generated by virtual vectors exhibit similar waveform features. Overall, this method allows us to explore the implicit relationships between different reflector features, providing valuable insights into the analysis of ice bottom conditions.

2.4 Feature Detection of Subglacial Water Bodies

185 We further investigate the distribution of different type's ice bottom reflectors in the radar images and their corresponding geometry features. We first note that a category of ice bottom reflectors synthesized by virtual vectors with symmetrical shapes and sharp, fast signal attenuation near the waveform peak (black waveform in Figure 3b, corresponding to black scatter plot in Figure 3a) is similar to existing classic subglacial water body reflector features (e.g., Schroeder et al., 2013; Hills et al., 2020). Furthermore, we trace the distribution of these reflectors in radar images. The results show that these reflectors are continuously

190 distributed in radar images, and the reflectors generally display flat, bright characteristics (Figure 4c). These continuous features are similar to the visual criteria used by glaciologists to identify subglacial lakes (Wolovick et al., 2013; Schroeder et al., 2013). Therefore, we further apply the results of the encoder-clustering as a candidate distribution of subglacial water bodies.

In further applications of observational data, it has been observed that the signal-to-noise ratio (SNR) of radar images from deep ice sheets is low due to the attenuation of radar signals. The interference of noise can occasionally cause odd

195 clusters in the detection of candidate subglacial water bodies (e.g., Figure 4c). Occasionally, subglacial water bodies may be mistakenly identified as appearing in non-water body areas. Additionally, the complex conditions of the ice bottom can also cause interruptions in subglacial lake detection. To eliminate noise interference and extract continuous subglacial lakes or water bodies, we limit the minimum width of subglacial water bodies in observational detection based on experimental experience. Detected subglacial water bodies should contain a continuous ice bottom segmentation in subglacial water type with a width

200 greater than 8 traces (corresponding to an average spatial distance of 10.4 m). Meanwhile, interruptions in continuous subglacial water bodies, which are narrower than 8 traces, are considered noise interference and will be interpolated and filled into nearby subglacial lakes. During interpolation, it is ensured that the interpolated non-subglacial water bodies in the continuous subglacial lakes are less than 25% to avoid interpolation artifacts due to specific noise.

By applying a threshold on the minimum width of subglacial water bodies, we obtain a list of candidate water bodies with

205 larger widths and reduce noise interference. However, some candidate water bodies still contain weak and blurry ice bottom reflector features that cannot be confirmed as subglacial water bodies. Therefore, we follow the conventional subglacial lake detection method based on englacial signal attenuation of bed reflectors (Wolovick et al., 2013; Hills et al., 2020). We apply a linear threshold filter based on the average peak reflector echo power in different depths to detect the reflector power anomalies. To simplify the process, we used the peak echo power directly from each reflector from the radar images. We consider the 2-D

210 distribution of ice thickness (depth) and peak echo power of subglacial reflectors recorded in the radar images (Figure 5) and
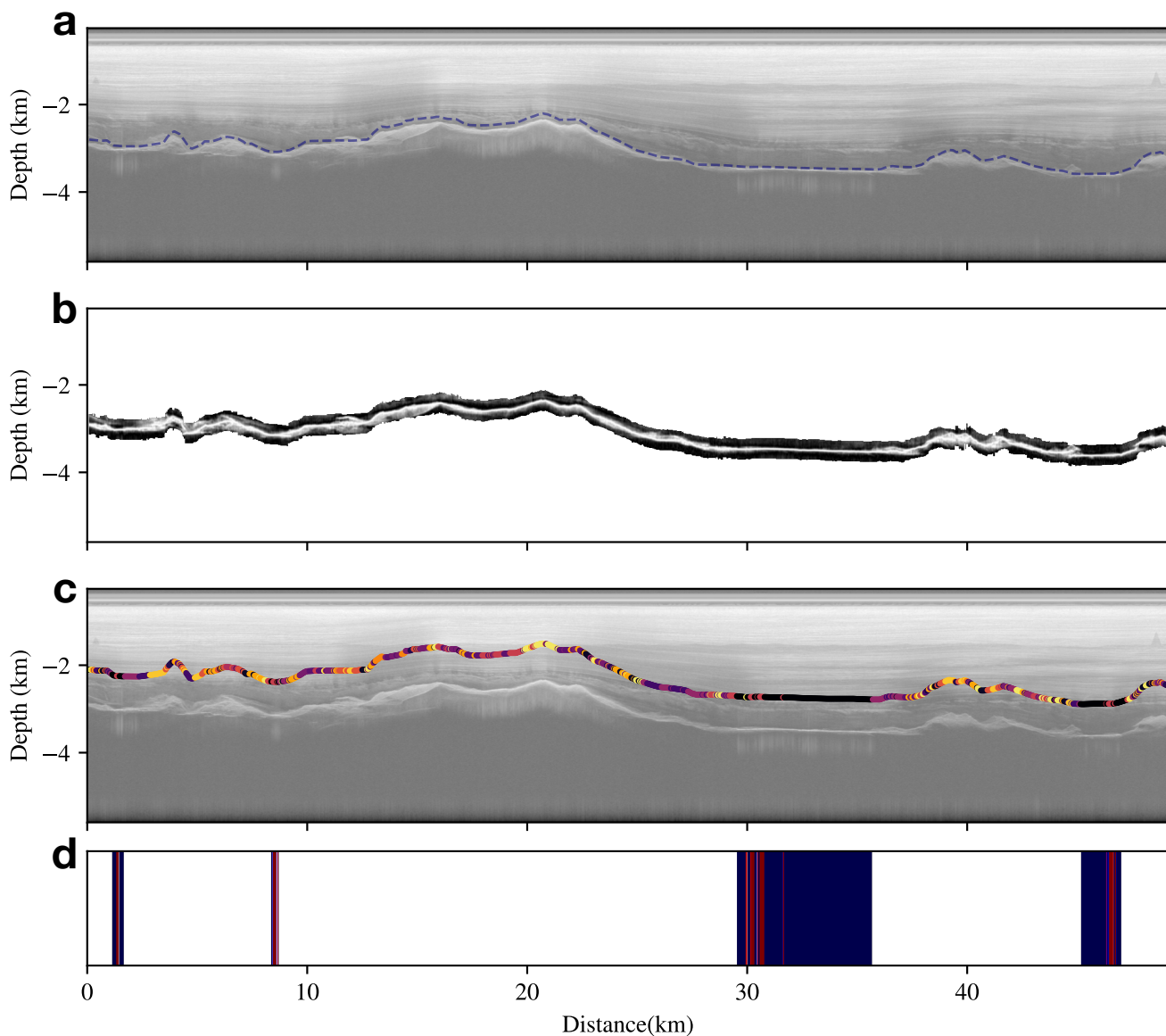
Figure 4. Example 1 of subglacial lake detection includes two larger and two smaller subglacial water bodies. (a) IPR image is shown with the blue dashed line indicating the positions of the ice bottom reflectors. (b) Separated, realigned, smoothed, denoised, and normalized ice bottom reflector features, which are applied as inputs to the encoder. (c) Unsupervised clustering results of the latent vectors obtained through encoding, where different colors correspond to classes in Figure 3. The black cluster corresponds to the candidate subglacial water bodies. (d) The subglacial water bodies detection based on continuous reflector features, where blue blocks represent the raw detected subglacial water bodies, and the red blocks are occasional interruptions that are filled by interpolation.

calculated the best linear fit and the standard deviation of the probability density. As the Z-axis (A-Scope) reflector features were considered in the previous steps, we obtained the average peak echo power for each detected candidate water body. Additionally, due to more reflector features used in the detection, a lower threshold in average echo power could be applied to detect more potential subglacial water bodies. We applied the best fit $+1\sigma$ as the threshold in different ice thickness, which was

215 lower than the threshold used in the previous study (Wolovick et al., 2013), to further confirm the candidate subglacial water bodies (as black points in Figure 5). The average echo power of the detected subglacial water bodies must be higher than the threshold. This step filters out the unconfirmed candidate water bodies with weak and blurry reflector features and improves the accuracy of the detection.
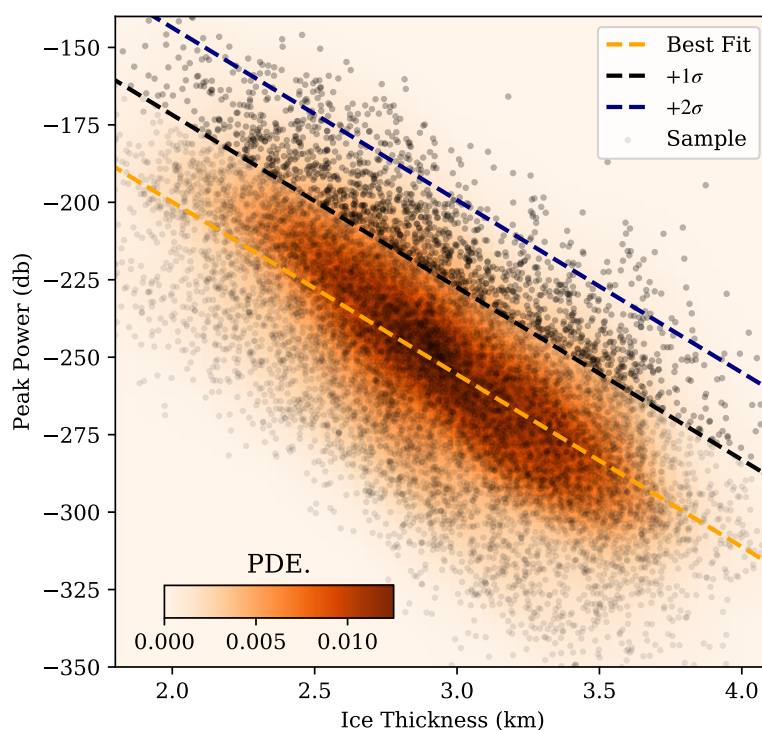
Figure 5. Distribution of ice bottom reflection peak power and ice thickness. The background colormap represents the probability density estimation (PDE.) of the data; orange dashed line represents the best linear fit; black and blue dashed lines denote the $+1\sigma$ and $+2\sigma$ cutoff thresholds, respectively. Gray dots represent reflector samples, while black dots represent the detected samples for subglacial water bodies.

3 Results

We apply the encode-cluster method to the IPR images in the AGAP-S database and trace the spatial distribution of subglacial water bodies in the images. In this section, we first demonstrate subglacial water bodies detected at different scales. Next, we compare the distribution of the detected subglacial water bodies with known lake inventories, and discuss the newly detected subglacial water bodies, as well as the known subglacial lakes missed by our method.

3.1 Subglacial Water Bodies in Different Scales

Figure 4 shows two large subglacial lake distributions and two smaller subglacial water bodies located at the bottom of subglacial valleys. The two larger lakes on the right display high return power as well as continuous and flat reflection features, which are relatively easy to detect visually. In contrast, the two smaller subglacial water bodies on the left are easily overlooked due to their relatively narrow widths containing insufficient continuous and flat reflection features. This example demonstrates the detection of two different types of subglacial lakes of varying widths from within a radar image. Due to the similarities in geothermal and subglacial environments in adjacent areas, the detection of the two smaller subglacial water bodies can be considered reliable based on the reflector encodes and the following clustering results. In addition to the examples shown in Figure 4, we provide further examples of subglacial water bodies detection in Figures 6 and 7, where the workflows and sequences applied are identical to those shown in Figure 4.

Figure 6 shows the detection of a relatively small subglacial water body, which is located at the concave bottom of a subglacial valley. Despite its short length, this water body displays a flat and continuous reflection interface, with strong return power and rapid attenuation characteristics, making it visually similar to the larger lakes in Figure 4 and Figure 7. The continuous reflection features of this type of smaller subglacial water bodies are narrower and less prominent, which makes them easily overlooked in visual detection in previous studies. However, the encode-cluster method based on reflector features from single trace can individually extract and classify each reflector sample, which enhances the detection sensitivity of this type of smaller subglacial water bodies.

Figure 7 presents a special example of a large continuous subglacial lake (about 40 km wide on the right) shown in a radar image. This subglacial lake has high returned power and flat reflection features that are visually easy to be detected. This subglacial lake has a visually obvious flat reflection feature with a high return power. However, only part of the lake is detected by the encode-cluster method based on reflector features, and discontinuities are found within the lake (Figure 7d). Upon inspecting the radar image (Figure 7a), we observe that the left part of this subglacial lake (indicated by the white arrow in Figure 7c) displays different reflector features from the detected part of the lake. These inconsistent features visually have relatively thick and uniform reflection layer-liked features near the ice bottom interface, resembling frozen-on ice as described by Bell et al. (2011). Additionally, another discontinuity interrupts the detected subglacial lake distribution in the center, which also implies thick reflection layer features. Moreover, in other areas of the radar image, there are also other continuous clusters of subglacial reflector features (as the yellow arrow indicates in Figure 7c). By tracing these clusters, we note that these different classes of reflectors correspond to distinct uniform reflection layers with varying thicknesses. Due to the similar features of
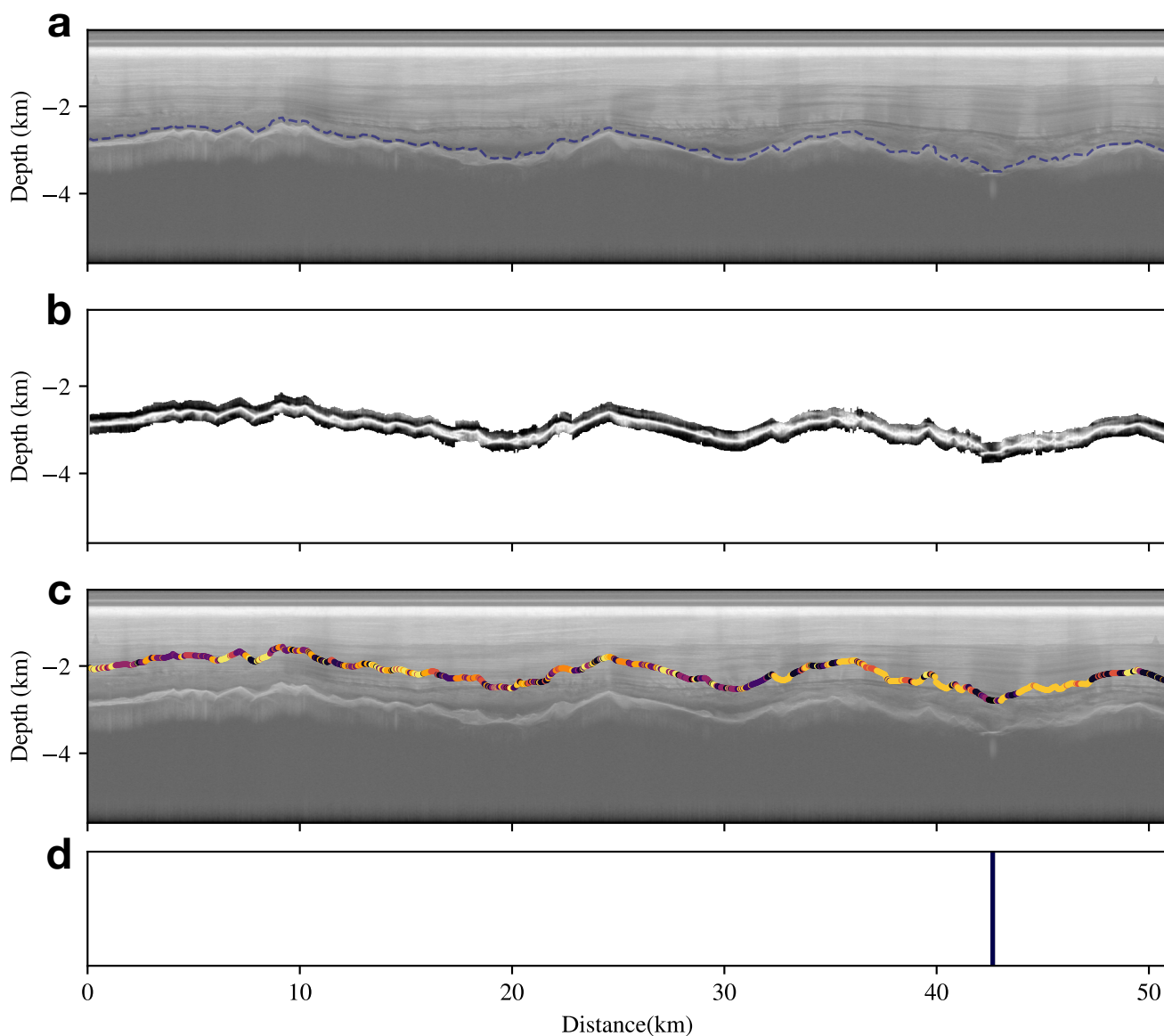
Figure 6. Example 2 of subglacial lake detection, which contains a relatively narrow subglacial water body. (a) Input radar image, where blue dashed line indicating the positions of the ice bottom reflectors. (b) Separated, realigned, smoothed, denoised, and normalized ice bottom reflector features, which are used as inputs to the encoder. (c) Unsupervised clustering results of the latent vectors obtained through encoding, where different colors correspond to classes in Figure 3. The black cluster corresponds to the candidate subglacial water bodies. (d) The subglacial water body detection based on continuous reflector features(blue block).
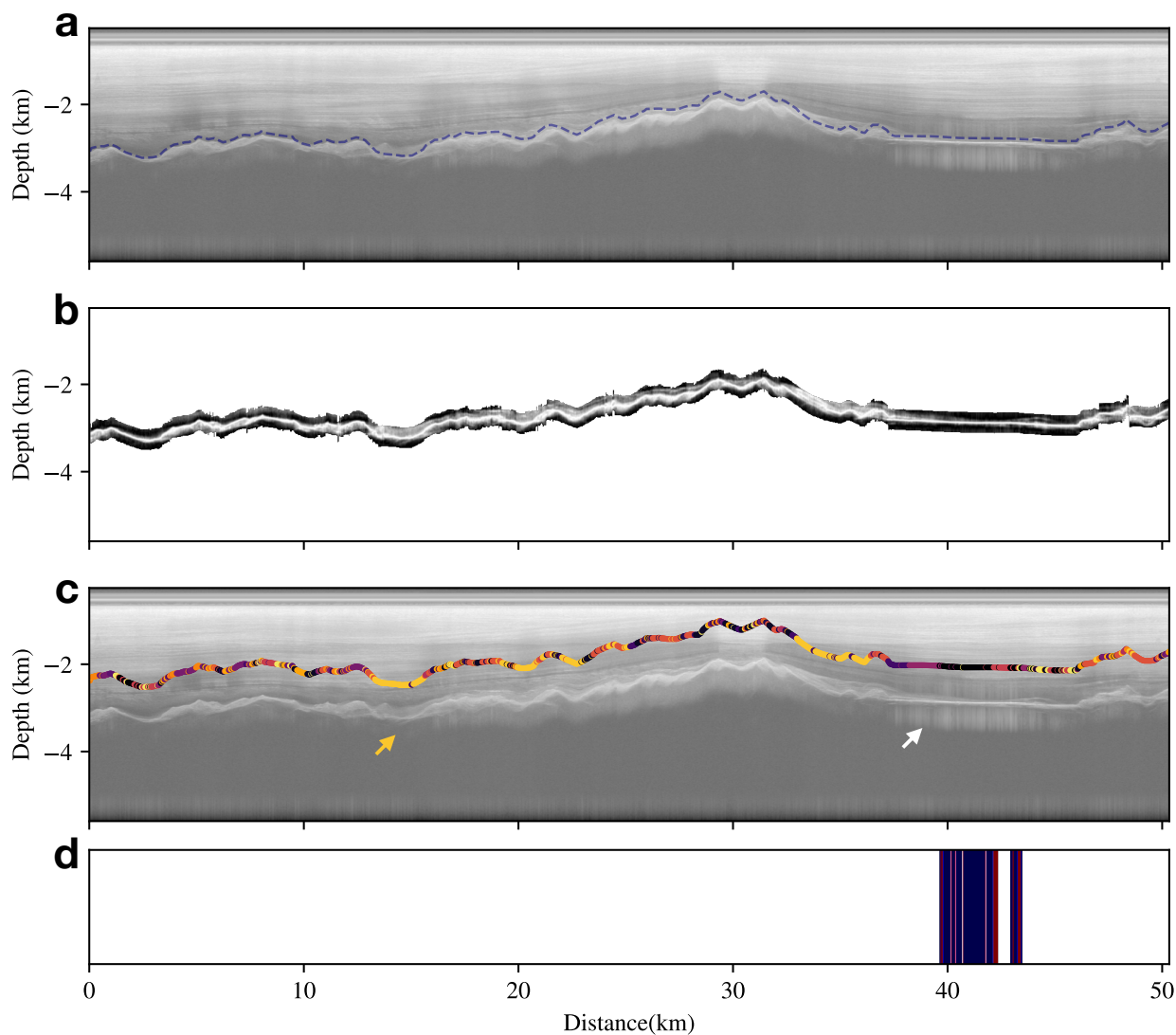
Figure 7. Example 3 of subglacial lake detection, which contains a subglacial water body. (a) Input radar image, where blue dashed line indicating the positions of the ice bottom reflectors. (b) Separated, realigned, smoothed, denoised, and normalized ice bottom reflector features, which are used as inputs to the encoder. (c) Unsupervised clustering results of the latent vectors obtained through encoding, where different colors correspond to classes in Figure 3. The black cluster corresponds to the candidate subglacial water bodies. (d) The subglacial water body detection based on continuous reflector features, where blue blocks represent the raw detected subglacial water bodies, and the red blocks are occasional interruptions filled by interpolation. Yellow arrow indicates another continus subglacial reflector class distribution, which may correspond to other symbolic subglacial conditions. White arrow indicates possible subglacial frozen-on ice condition.

ice bottom reflections, we suggest that these continuous spatial distributions may relate to the ice flow dynamics and different stages of frozen-on ice (Bell et al., 2011).

3.2 Spatial Distribution of Detected Subglacial Lakes

255 We compile and integrate the identified subglacial lakes and water bodies from the AGAP-S IPR images, and locate each detection within the spatial sampling range of each radar image provided by the database. Figure 8 presents the spatial distribution of subglacial water bodies detected in the Gamburtsev Subglacial Mountains region, where the blue points represent subglacial water bodies that have been confirmed by applying an average peak reflection power filter to subglacial water body candidates detected by the encode-cluster method (cyan points in Figure 8). Overall, the subglacial water bodies are distributed in clusters

260 with spatial continuity (e.g., the regional cluster near L1 and L3 area), but some are also sparsely detected.

In addition to the subglacial lakes detected in this study, we compare the previously identified subglacial lake distributions, as shown by the red and yellow points in Figure 8, which correspond to the inventories of Wolovick et al. (2013) and Livingstone et al. (2022), respectively. The two larger subglacial lakes (shown in Figure 4 and 7) correspond to the known subglacial lakes listed in the inventories (labeled as L1 and L3 in Figure 8). In contrast, the narrow subglacial water body shown in Figure

265 6 is not previously included in the inventories (labeled as L2 in Figure 8), which is newly detected. Overall, the subglacial lake distribution detected in this study roughly overlaps with the known inventory, but there are also some mismatches, such as the lines labeled E1-E5 and N1-N4 in Figure 8. To further investigate the reasons for these discrepancies, we select the corresponding radar image segments from labeled regions and plot the segments in Figure 9 and 10, respectively.

Figure 9 displays segments of radar images from the N1-N4 subregions, revealing multiple new subglacial water bodies

270 detected by the new method (indicated as blue lines in Figures 9). Figure 9a illustrates two detected subglacial water bodies, one on the left (marked as orange line below) that was already included in previous subglacial lake inventories, and one on the right that is newly detected by the new method. The ice bottom reflectors of both subglacial water bodies have a similar visual appearance, with sharp and narrow reflectors in the Z-axis. However, the water body on the right has a narrower width, which could make it easier to overlook visually, potentially causing it to be neglected in previous studies. The radar segment displayed

275 in Figure 9b is from the N2 subregion near -83°S, 70°E in Figure 8, where a group of continuous subglacial water bodies has been detected and recorded in the known inventory. The new method detects subglacial lakes in about 7 km in Figure 9b, while multiple reflectors with thick layer features (marked by red arrows) display in the 16 and 29 km simultaneously. Considering the dense distribution of subglacial water bodies nearby, these thicker reflection features are possibly formed by frozen-on ice due to ice flow. Figures 9c and d show several smaller subglacial water bodies, which are similar to the narrow subglacial water

280 body shown in example 2 in Figure 6. These small water bodies may have originated from local melting or subglacial rivers, corresponding to the sparse but regionally dense distribution of subglacial water bodies in the L2, N3 and N4 regions in Figure 8.

Figure 10 presents subglacial lakes previously identified in the inventories, but which are not accurately detected by the encode-cluster method and return power filtering. The orange arrows in Figure 10 indicate the locations of previously identified

285 subglacial lakes. In Figure 10a, although there are multiple candidate water bodies in the E1 subregion from the encode-
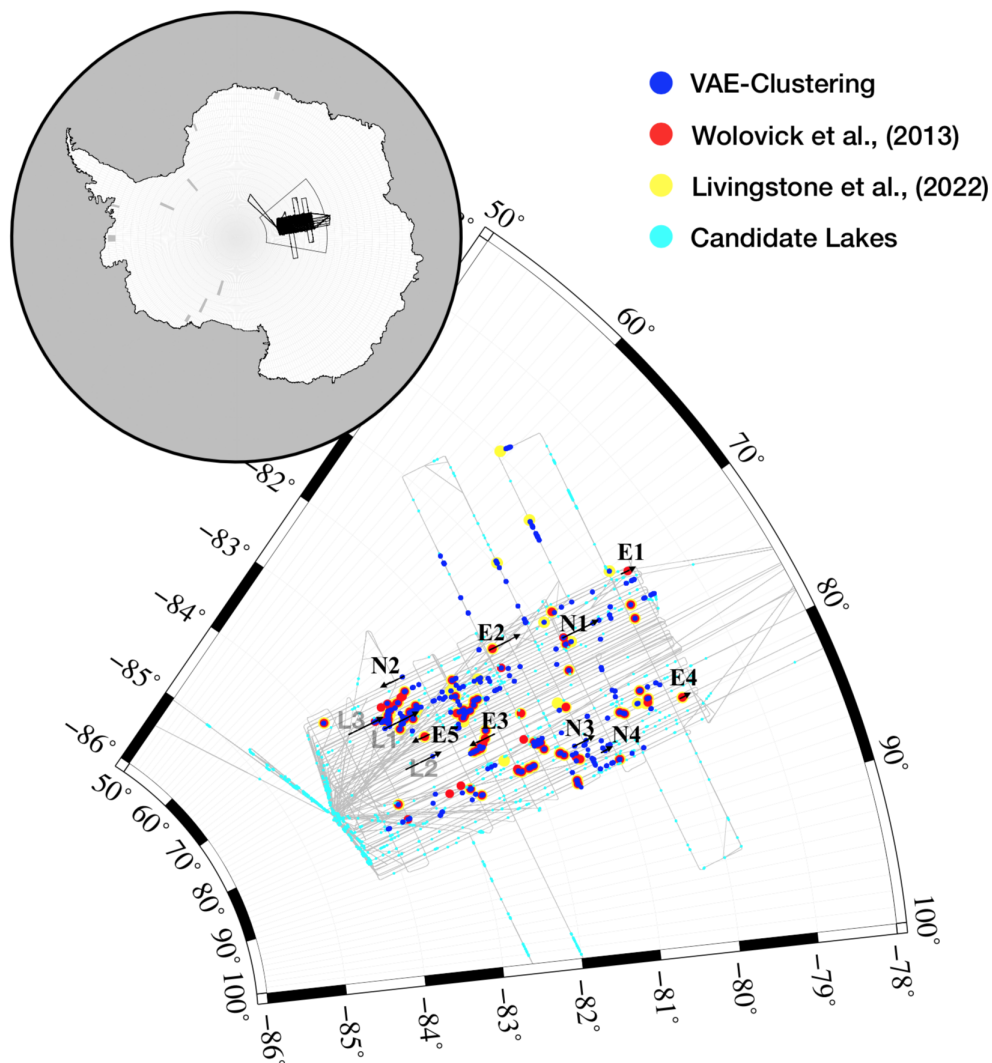
Figure 8. Distribution of airborne radar observation lines and detected subglacial water bodies in the Gamburtsev Subglacial Mountains region. Blue points indicate the distribution of subglacial water bodies detected in this study. Cyan points mark the water body candidates from the encode-cluster method. Red and yellow points mark the subglacial lake distribution from the subglacial lake inventory from Wolovick et al. (2013) and Livingstone et al. (2022), respectively. Text labels and arrows indicate the positions and directions of selected airborne radar observation lines, with survey lines of Figures 4, 6 and 7 labeled as L1, L2, and L3, respectively. The inset map shows the location of the study area.
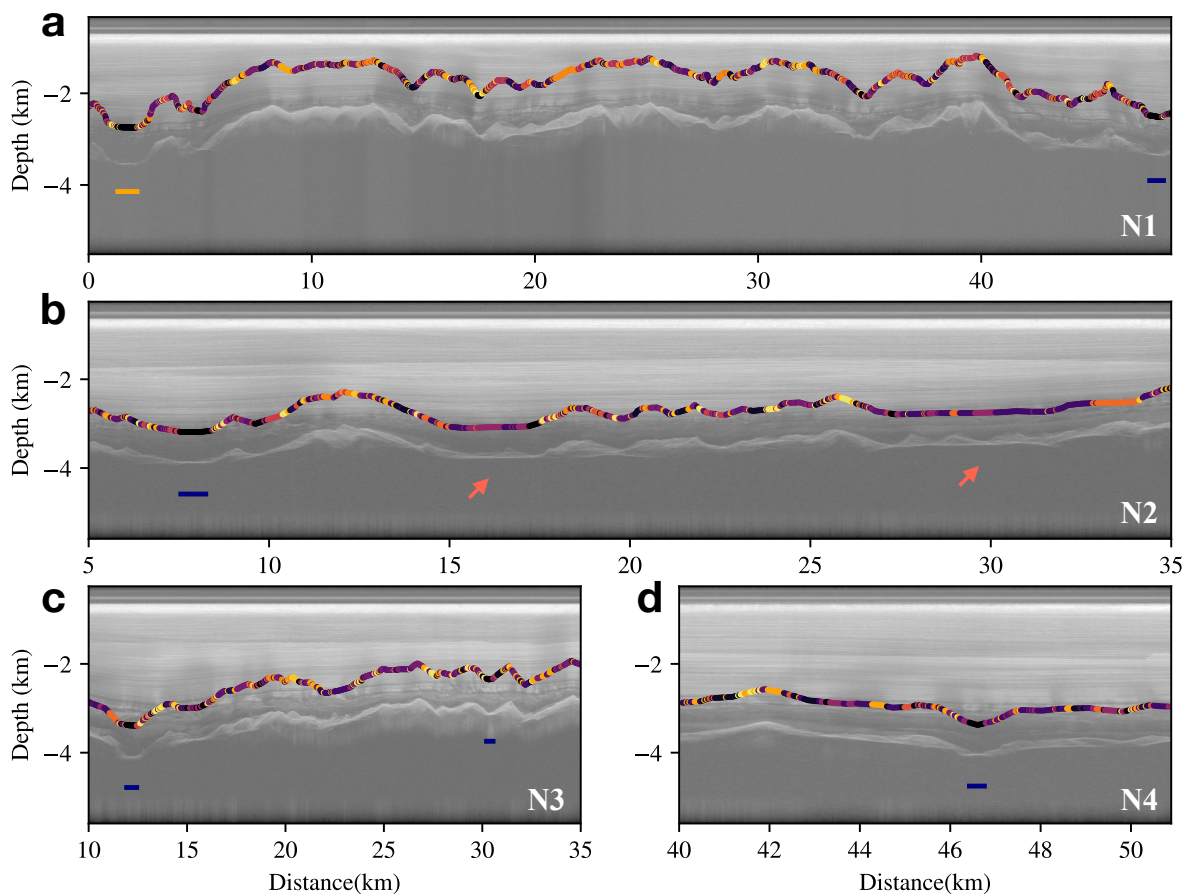
Figure 9. Newly detected subglacial lakes and water bodies in the Gamburtsev Subglacial Mountains region, with text labels corresponding to the location distribution in Figure 8. Scatter points in different colors mark the encoded classes of the ice bottom reflectors, and the blue and orange lines indicate the detected range of subglacial water bodies or lakes. (a) IPR image of the N1 region, containing a known subglacial lake (orange line on the left) and a newly detected subglacial lake (right). (b) Radar image segment of the N2 region, containing a newly labeled subglacial lake area; the two relatively flat ice bottom reflection segments indicated by red arrows may record the frozen-on ice. (c-d) Newly detected regional subglacial water bodies with smaller sizes, from radar image segments from the N3 and N4 regions, respectively.

clustering in the radar segment, the average peak power is insufficient to confirm the subglacial lake in each water body candidate. The ice bottom reflectors of this radar segment differ visually from other known subglacial lake features (e.g., Figures 4, 7 and 9). In Figure 10b, the ice bottom reflectors near known subglacial lakes are classified as corresponding to other reflector classes instead of water body reflectors. By inspecting the radar image, these reflectors display a thick layer near the ice bottom reflections, which are similar to reflections in Figure 7c. We consider that the subglacial lake in this segment may correspond to a frozen-on ice condition. Similarly, the reflectors from previously identified subglacial lakes in the E4 and E5 subregions in Figures 10d and e are also classified as other ice bottom reflection classes by the encode-cluster method.
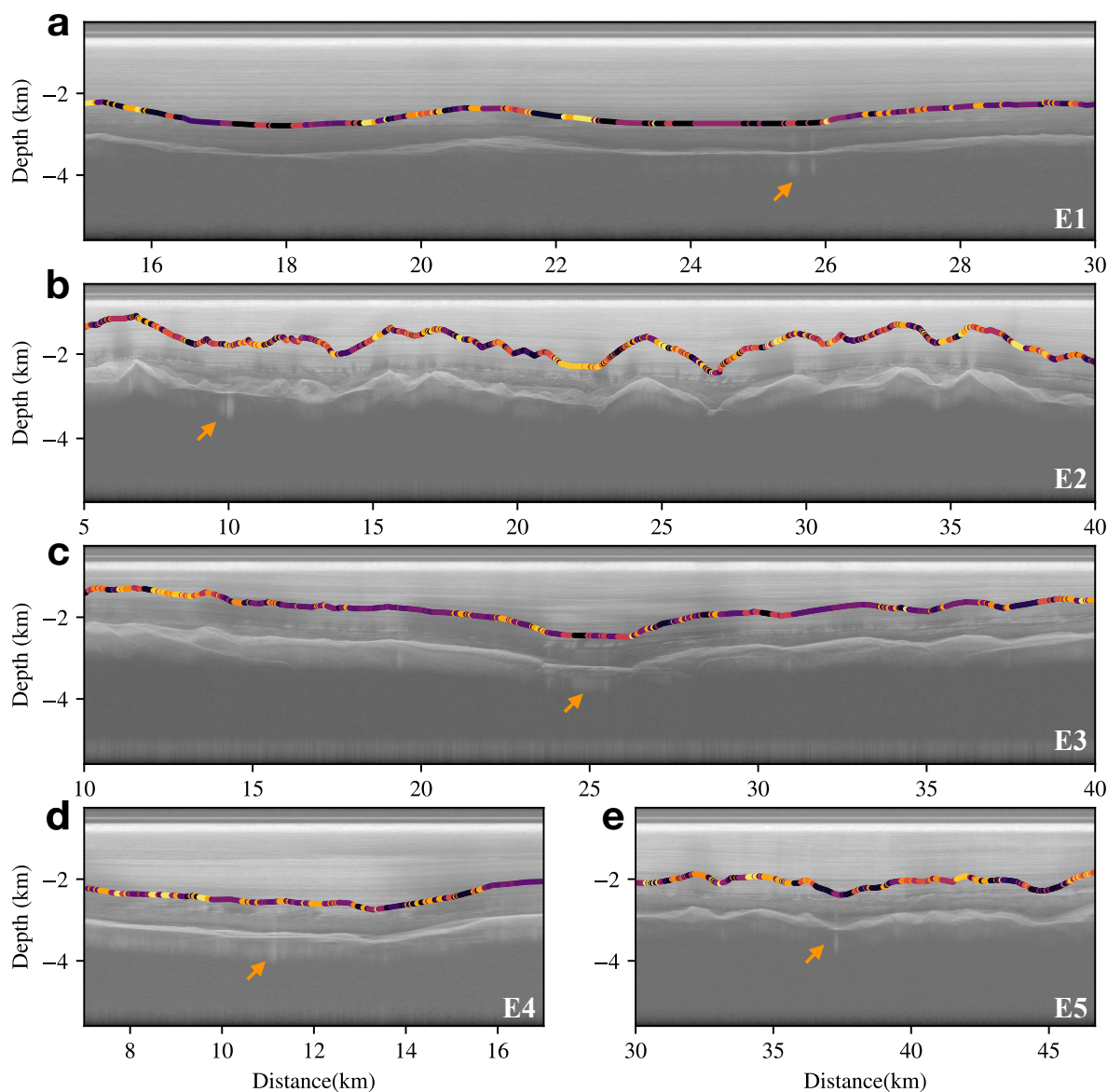
Figure 10. IPR image segments from the Gamburtsev Subglacial Mountains area, which mismatch with the identified lake inventory (Wolovick et al., 2013; Livingstone et al., 2022). The text labels correspond to the locations marked in Figure 8, and orange arrows mark the locations of the identified subglacial lakes from the inventories.

By observing the radar image segments corresponding to these two subregions, the ice bottom reflectors that corresponded to previously identified subglacial lakes also display thicker layer reflections, which do not match other subglacial lake features from other regions. The undetected subglacial water body in Figure 10c, near 25 km, is similar to Figure 10a, where the average

return power is insufficient to confirm the subglacial lakes. Besides, the encoded classes of ice bottom reflectors near the white arrow change to other classes, indicating that the potential lakes here may consist of more complex bottom conditions.

Overall, the new method in this study can capture more candidate subglacial water bodies with similar reflector features to the previous lake inventories. Compared to the previously identified lake inventories, most of the newly detected subglacial lakes or water bodies in this study are smaller subglacial water bodies, which are more easily overlooked visually and possibly difficult to be extracted by multi-trace detection methods. The undetected subglacial lakes compared with known inventories may be caused by the complex basal conditions formed by ice flow, which results in thicker reflection features in radar images. These thicker reflectors may also correspond to other subglacial conditions, which still need further investigation by drilling or modeling.

4 Discussion

The subglacial analysis method proposed in this study is based on the shape of the ice bottom reflector features, which enables full exploitation of all the reflection information contained in the IPR observation data, providing a novel observational perspective for the study of the ice bottom beyond reflection power intensity and roughness. Moreover, the distance between vectors in the latent space can serve as a statistical similarity indicator for reflector features. The unsupervised clustering analysis applied in the latent vectors relies on the implied feature difference of the reflection waveform, effectively excluding subjective and external factors in finding potential classifications of subglacial conditions, and reducing the dependence on model assumptions. By contrast, this study does not use manual labels, thereby minimizing the potential for artificial misfit in the detection of subglacial water bodies and allowing for the application of this approach in surveying other subglacial conditions.

In this study, the final subglacial water bodies are obtained using radar echo power filtering, which is based on the linear relationship between reflection power and ice thickness (depth of ice bottom). However, this simple linear threshold filtering potentially excludes subglacial water bodies with weaker echo power. To improve the detection of weaker subglacial lake signals, more precise filtering strategies that take into account the roughness and slope of the ice bottom may be beneficial.

Although the encode-cluster method provides an abstract classification for ice bottom reflections, the physical properties of the ice bottom reflection and the corresponding cluster still require further interpretation. The VAE encoder maps high-dimensional reflections to a vector that map to the reflector waveform feature. In the future, physical modeling and in-situ drilling may provide more direct relationships between the latent vectors and subglacial conditions, thereby enhancing the understanding of this subglacial lake detection method.

In addition to subglacial water bodies, other clusters of ice bottom reflections also exhibit some consistent patterns, as illustrated in Figures 7, 9b, and 10b. These resemblances may originate from similar subglacial conditions, particularly the thick layer-like reflections that could correspond to different stages of frozen-on ice. The encode-cluster method is capable of isolating these reflection clusters, offering potential data for studying glacier dynamics. Geostatistical modeling based on subglacial topography (MacKie et al., 2020) may provide additional references for the reflector clusters in corresponding

subglacial conditions. In addition, the novel interpretation of latent clustering may enhance the conventional geostatistical analysis.

330   The detection method used in this study is based on deep learning, allowing for the automated analysis data. Deep learning extractors, such as EisNet (Dong et al., 2021), developed in recent years can efficiently pick up the bed interface in radar images. By combining these two types of DL methods, an automatic method can be implemented to first extract the positions of the ice bottom and then analyze the features of the bottom reflector, which can further update the subglacial lake inventory by applying this combined DL method in the available IPR database. The data used in this study is focused on the Gamburtsev Subglacial

335   Mountains and can be extended to other database's radar image analyses covering the Arctic, Antarctic, and Qinghai-Tibet Plateau. it has potential applications for analyzing and tracing spatiotemporal changes in global subglacial water bodies and other ice bottom reflection features. Furthermore, this method based on radar signal analysis can also provide classifications for single-track radar data, and can be independently applied to this type of radar data such as A-Scope observations. The VAE-cluster method trained on Earth data also provides a reference for analyzing ice bottom reflection in Mars satellite radar

340   observations.

5   Conclusions

We constructed a dataset of ice bottom reflection signals based on IPR data from the Gamburtsev Subglacial Mountains region in the CReSIS database. Using the VAE, we encoded and reconstructed the reflection signal features in the dataset. By applying K-means clustering to the encoded features, we separated the reflector features corresponding to subglacial lakes. By consid-

345   ering the relationship between the peak reflection power and ice thickness, we filtered subglacial lake candidates in this region. Compared with existing inventories, our method can effectively detect features of subglacial water bodies and extract more smaller subglacial lakes. This method has potential applications in expanding the subglacial lake inventory and interpreting other subglacial conditions.

Data availability.   The IPR images and bed echo markers used in this study were obtained from the CReSIS (Center for Remote Sensing of

350   Ice Sheets) database at https://cresis.ku.edu/.

Author contributions.   SD, LF and XT conceptualized the study. SD, LF and ZL implemented the methods and analysis. SD, LF, XT and XC interpreted the results. SD, LF and XT wrote the manuscript with corrections from ZL and XC.

Competing interests.   The authors acknowledge there are no conflicts of interest recorded.

Acknowledgements. This study was supported by the National Natural Science Foundation of China (Nos. 42276257, 41941006, 41974044)
and the National Key Research and Development Program of China (No.2021YFC2801404). The authors would like to express their gratitude
to A.Prof. Dustin Schroeder from Stanford University and Prof. Tong Hao from Tongji University for their valuable suggestions on this work.

References

Arnold, E., Leuschen, C., Rodriguez-Morales, F., Li, J., Paden, J., Hale, R., and Keshmiri, S.: CReSIS airborne radars and platforms for ice and snow sounding, Annals of Glaciology, 61, 58–67, 2020.

Bell, R. E., Ferraccioli, F., Creyts, T. T., Braaten, D., Corr, H., Das, I., Damaske, D., Frearson, N., Jordan, T., Rose, K., et al.: Widespread persistent thickening of the East Antarctic Ice Sheet by freezing from the base, Science, 331, 1592–1595, 2011.

Bowling, J., Livingstone, S., Sole, A., and Chu, W.: Distribution and dynamics of Greenland subglacial lakes, Nature communications, 10, 1–11, 2019.

Carter, S. P., Blankenship, D. D., Peters, M. E., Young, D. A., Holt, J. W., and Morse, D. L.: Radar-based subglacial lake classification in Antarctica, Geochemistry, Geophysics, Geosystems, 8, 2007.

Cheng, X. and Jiang, K.: Crustal model in eastern Qinghai-Tibet plateau and western Yangtze craton based on conditional variational autoencoder, Physics of the Earth and Planetary Interiors, 309, 106 584, 2020.

Christner, B. C., Priscu, J. C., Achberger, A. M., Barbante, C., Carter, S. P., Christianson, K., Michaud, A. B., Mikucki, J. A., Mitchell, A. C., Skidmore, M. L., et al.: A microbial ecosystem beneath the West Antarctic ice sheet, Nature, 512, 310–313, 2014.

Dong, S., Tang, X., Guo, J., Fu, L., Chen, X., and Sun, B.: EisNet: Extracting Bedrock and Internal Layers from Radiostratigraphy of Ice Sheets with Machine Learning, IEEE Transactions on Geoscience and Remote Sensing, 60, 1–12, 2021.

Dowdeswell, J. A. and Evans, S.: Investigations of the form and flow of ice sheets and glaciers using radio-echo sounding, Reports on Progress in Physics, 67, 1821, 2004.

Dowdeswell, J. A. and Siegert, M. J.: The dimensions and topographic setting of Antarctic subglacial lakes and implications for large-scale water storage beneath continental ice sheets, Geological Society of America Bulletin, 111, 254–263, 1999.

Esfahani, R. D. D., Vogel, K., Cotton, F., Ohrnberger, M., Scherbaum, F., and Kriegerowski, M.: Exploring the Dimensionality of Ground-Motion Data by Applying Autoencoder Techniques, Bulletin of the Seismological Society of America, 111, 1563–1576, 2021.

Fettweis, X., Franco, B., Tedesco, M., Van Angelen, J., Lenaerts, J. T., van den Broeke, M. R., and Gallée, H.: Estimating the Greenland ice sheet surface mass balance contribution to future sea level rise using the regional atmospheric climate model MAR, The Cryosphere, 7, 469–489, 2013.

Gades, A. M., Raymond, C. F., Conway, H., and Jagobel, R.: Bed properties of Siple Dome and adjacent ice streams, West Antarctica, inferred from radio-echo sounding measurements, Journal of Glaciology, 46, 88–94, 2000.

García, M. H., Donini, E., and Bovolo, F.: Automatic segmentation of ice shelves with deep learning, in: 2021 IEEE International Geoscience and Remote Sensing Symposium IGARSS, pp. 4833–4836, IEEE, 2021.

Ghosh, R. and Bovolo, F.: TransSounder: A hybrid TransUNet-TransFuse architectural framework for semantic segmentation of radar sounder data, IEEE Transactions on Geoscience and Remote Sensing, 60, 1–13, 2022.

Gifford, C. M. and Agah, A.: Subglacial water presence classification from polar radar data, ENGINEERING APPLICATIONS OF ARTIFICIAL INTELLIGENCE, 25, 853–868, https://doi.org/10.1016/j.engappai.2011.12.002, 2012.

Hao, T., Jing, L., Liu, J., Wang, D., Feng, T., Zhao, A., and Li, R.: Automatic Detection of Subglacial Water Bodies in the AGAP Region, East Antarctica, Based on Short-Time Fourier Transform, Remote Sensing, 15, 363, 2023.

Hills, B. H., Christianson, K., and Holschuh, N.: A framework for attenuation method selection evaluated with ice-penetrating radar data at south pole lake, Annals of Glaciology, 61, 176–187, 2020.

Ilisei, A.-M. and Bruzzone, L.: A system for the automatic classification of ice sheet subsurface targets in radar sounder data, IEEE Transactions on Geoscience and Remote Sensing, 53, 3260–3277, 2015.

395 Ilisei, A.-M., Khodadadzadeh, M., Ferro, A., and Bruzzone, L.: An automatic method for subglacial lake detection in ice sheet radar sounder data, IEEE Transactions on Geoscience and Remote Sensing, 57, 3252–3270, 2018.

Kamb, B.: Glacier surge mechanism based on linked cavity configuration of the basal water conduit system, Journal of Geophysical Research: Solid Earth, 92, 9083–9100, 1987.

Key, K. and Siegfried, M. R.: The feasibility of imaging subglacial hydrology beneath ice streams with ground-based electromagnetics,
400 Journal of Glaciology, 63, 755–771, 2017.

King, M. D., Howat, I. M., Candela, S. G., Noh, M. J., Jeong, S., Noël, B. P., van den Broeke, M. R., Wouters, B., and Negrete, A.: Dynamic ice loss from the Greenland Ice Sheet driven by sustained glacier retreat, Communications Earth & Environment, 1, 1–7, 2020.

Kingma, D. P. and Ba, J.: Adam: A method for stochastic optimization, arXiv preprint arXiv:1412.6980, 2014.

Kingma, D. P. and Welling, M.: Auto-encoding variational bayes, arXiv preprint arXiv:1312.6114, 2013.

405 Lang, S., Yang, M., Cui, X., Li, L., Cai, Y., Liu, X., Guo, J., Sun, B., and Siegert, M.: A Semiautomatic Method for Predicting Subglacial Dry and Wet Zones Through Identifying Dry–Wet Transitions, IEEE Transactions on Geoscience and Remote Sensing, 60, 1–15, 2022.

Li, H. and Misra, S.: Prediction of subsurface NMR T2 distributions in a shale petroleum system using variational autoencoder-based neural networks, IEEE Geoscience and Remote Sensing Letters, 14, 2395–2397, 2017.

Li, Z.: A generic model of global earthquake rupture characteristics revealed by machine learning, Geophysical Research Letters, 49,
410 e2021GL096 464, 2022.

Liu, M., Grana, D., and de Figueiredo, L. P.: Uncertainty quantification in stochastic inversion with dimensionality reduction using variational autoencoder, Geophysics, 87, M43–M58, 2022.

Liu-Schiaffini, M., Ng, G., Grima, C., and Young, D.: Ice Thickness From Deep Learning and Conditional Random Fields: Application to Ice-Penetrating Radar Data With Radiometric Validation, IEEE Transactions on Geoscience and Remote Sensing, 60, 1–14, 2022.

415 Livingstone, S. J., Li, Y., Rutishauser, A., Sanderson, R. J., Winter, K., Mikucki, J. A., Björnsson, H., Bowling, J. S., Chu, W., Dow, C. F., et al.: Subglacial lakes and their changing role in a warming climate, Nature Reviews Earth & Environment, 3, 106–124, 2022.

Lopez-Alvis, J., Laloy, E., Nguyen, F., and Hermans, T.: Deep generative models in inversion: The impact of the generator's nonlinearity and development of a new approach based on a variational autoencoder, Computers & Geosciences, 152, 104 762, 2021.

Ma, S., Li, Z., and Wang, W.: Machine learning of source spectra for large earthquakes, Geophysical Journal International, 231, 692–702,
420 2022.

MacKie, E., Schroeder, D., Caers, J., Siegfried, M., and Scheidt, C.: Antarctic topographic realizations and geostatistical modeling used to map subglacial lakes, Journal of Geophysical Research: Earth Surface, 125, e2019JF005 420, 2020.

MacQueen, J.: Classification and analysis of multivariate observations, in: 5th Berkeley Symp. Math. Statist. Probability, pp. 281–297, University of California Los Angeles LA USA, 1967.

425 Mikucki, J. A., Lee, P., Ghosh, D., Purcell, A., Mitchell, A. C., Mankoff, K., Fisher, A., Tulaczyk, S., Carter, S., Siegfried, M. R., et al.: Subglacial Lake Whillans microbial biogeochemistry: a synthesis of current knowledge, Philosophical Transactions of the Royal Society A: Mathematical, Physical and Engineering Sciences, 374, 20140 290, 2016.

Oswald, G. and Robin, G. d.: Lakes beneath the Antarctic ice sheet, Nature, 245, 251–254, 1973.

Paden, J., Akins, T., Dunson, D., Allen, C., and Gogineni, P.: Ice-sheet bed 3-D tomography, Journal of Glaciology, 56, 3–11, 2010.

430   Pattyn, F.: Antarctic subglacial conditions inferred from a hybrid ice sheet/ice stream model, Earth and Planetary Science Letters, 295, 451–461, 2010.

Rahnemoonfar, M., Fox, G. C., Yari, M., and Paden, J.: Automatic ice surface and bottom boundaries estimation in radar imagery based on level-set approach, IEEE Transactions on Geoscience and Remote Sensing, 55, 5115–5122, 2017.

Robin, G. d. Q., Swithinbank, C., Smith, B., et al.: Radio echo exploration of the Antarctic ice sheet, International Association of Scientific
435   Hydrology Publication, 86, 97–115, 1970.

Schroeder, D. M., Blankenship, D. D., and Young, D. A.: Evidence for a water system transition beneath Thwaites Glacier, West Antarctica, Proceedings of the National Academy of Sciences, 110, 12 225–12 228, 2013.

Siegert, M. J.: Antarctic subglacial lakes, Earth-Science Reviews, 50, 29–50, 2000.

Siegert, M. J. and Ridley, J. K.: Determining basal ice-sheet conditions in the Dome C region of East Antarctica using satellite radar altimetry
440   and airborne radio-echo sounding, Journal of Glaciology, 44, 1–8, 1998.

Siegfried, M. R., Fricker, H. A., Carter, S. P., and Tulaczyk, S.: Episodic ice velocity fluctuations triggered by a subglacial flood in West Antarctica, Geophysical Research Letters, 43, 2640–2648, 2016.

Smith, A. M., Woodward, J., Ross, N., Bentley, J., Hodgson, D. A., Siegert, M. J., and King, E. C.: Evidence for the long-term sedimentary environment in an Antarctic subglacial lake, Earth and Planetary Science Letters, 504, 139–151, 2018.

445   Stearns, L. A., Smith, B. E., and Hamilton, G. S.: Increased flow speed on a large East Antarctic outlet glacier caused by subglacial floods, Nature Geoscience, 1, 827–831, 2008.

Studinger, M., Bell, R. E., and Tikku, A. A.: Estimating the depth and shape of subglacial Lake Vostok's water cavity from aerogravity data, Geophysical Research Letters, 31, 2004.

Tang, X., Luo, K., Dong, S., Zhang, Z., and Sun, B.: Quantifying Basal Roughness and Internal Layer Continuity Index of Ice Sheets by an
450   Integrated Means with Radar Data and Deep Learning, Remote Sensing, 14, 4507, 2022.

Varshney, D., Rahnemoonfar, M., Yari, M., and Paden, J.: Deep ice layer tracking and thickness estimation using fully convolutional networks, in: 2020 IEEE International Conference on Big Data (Big Data), pp. 3943–3952, IEEE, 2020.

Varshney, D., Rahnemoonfar, M., Yari, M., Paden, J., Ibikunle, O., and Li, J.: Deep learning on airborne radar echograms for tracing snow accumulation layers of the Greenland ice sheet, Remote Sensing, 13, 2707, 2021.

455   Wang, H., Tang, X., Xiao, E., Luo, K., Dong, S., and Sun, B.: Basal Melt Patterns around the Deep Ice Core Drilling Site in the Dome A Region from Ice-Penetrating Radar Measurements, Remote Sensing, 15, 1726, 2023.

Wolovick, M. J., Bell, R. E., Creyts, T. T., and Frearson, N.: Identification and control of subglacial water networks under Dome A, Antarctica, JOURNAL OF GEOPHYSICAL RESEARCH-EARTH SURFACE, 118, 140–154, https://doi.org/10.1029/2012JF002555, 2013.

Xu, M., Crandall, D. J., Fox, G. C., and Paden, J. D.: Automatic estimation of ice bottom surfaces from radar imagery, in: 2017 IEEE
460   International Conference on Image Processing (ICIP), pp. 340–344, IEEE, 2017.

Yari, M., Rahnemoonfar, M., and Paden, J.: Multi-scale and temporal transfer learning for automatic tracking of internal ice layers, in: IGARSS 2020-2020 IEEE International Geoscience and Remote Sensing Symposium, pp. 6934–6937, IEEE, 2020.

Zeising, O., Steinhage, D., Nicholls, K. W., Corr, H. F., Stewart, C. L., and Humbert, A.: Basal melt of the southern Filchner Ice Shelf, Antarctica, The Cryosphere, 16, 1469–1482, 2022.